

# Regulating cellular metabolism and morphology to achieve high-yield synthesis of hyaluronan with controllable molecular weights

Received: 15 August 2024

Accepted: 6 February 2025

Published online: 28 February 2025



Litao Hu<sup>1,2,3,4,5,6</sup>, Sen Xiao<sup>1,2,3,4</sup>, Jieyu Sun<sup>1,2,3,4</sup>, Faying Wang<sup>1,2,4</sup>,  
Guobin Yin<sup>1,2,3,4</sup>, Wenjie Xu<sup>1,2,3,4</sup>, Jianhua Cheng<sup>5,6</sup>, Guocheng Du<sup>1,2,4</sup>,  
Jian Chen<sup>1,2,3,4,5</sup> & Zhen Kang<sup>1,2,3,4,5</sup> ✉

High-yield biosynthesis of hyaluronan (HA) with controllable molecular weights (MWs) remains challenging due to the poorly understood function of Class I HA synthase (HAS) and the metabolic imbalance between HA biosynthesis and cellular growth. Here, we systematically characterize HAS to identify crucial regions involved in HA polymerization, secretion, and MW control. We construct HAS mutants that achieve complete HA secretion and expand the MW range from 300 to 1400 kDa. By dynamically regulating UDP-glucose 6-dehydrogenase activity and applying an adaptive evolution approach, we recover cell normal growth with increased metabolic capacities. Final titers and productivities for high MW HA (500 kDa) and low MW HA (10 kDa) reach 45 g L<sup>-1</sup> and 105 g L<sup>-1</sup>, 0.94 g L<sup>-1</sup> h<sup>-1</sup> and 1.46 g L<sup>-1</sup> h<sup>-1</sup>, respectively. Our findings advance our understanding of HAS function and the interplay between cell metabolism and morphology, and provide a shape-guided engineering strategy to optimize microbial cell factories.

Hyaluronan (HA), a linear, non-sulfated glycosaminoglycan composed of repeating disaccharide units of  $\beta$ -(1,4)-N-acetylglucosamine (GlcNAc) and  $\beta$ -(1,3)-glucuronic acid (GlcA), is widely distributed in the extracellular matrix of vertebrates<sup>1,2</sup>. Naturally, HA is produced by a limited number of bacteria, viruses, and fungi<sup>2</sup>. Because of its physicochemical properties, including viscosity, elasticity, lubrication, and high water-holding capacity, and its biological functions such as promoting wound healing, regulating immune function, and modulating the inflammatory response, various HA with different molecular weights (MWs) and its derivatives have been used in cosmetic, pharmaceutical, biomedical, and food industries<sup>3–5</sup>. The physicochemical properties and biological effects of HA largely depend on its MW<sup>1,2</sup>. High-molecular-weight HA (typically greater than 1000 kDa), is widely

used as a visco-supplement in osteoarthritis treatment and eye surgeries because of its high resistance to degradation and viscoelastic and supportive properties<sup>2</sup>. Medium- to high-molecular-weight HA (typically between 50 and 1000 kDa) exhibits excellent moisturizing and repair capabilities and is extensively utilized in cosmetics for deep hydration and skin repair. Low-molecular-weight HA (typically below 50 kDa) can inhibit multidrug resistance in tumors, induce angiogenesis, and cause inflammation, thus making it valuable in medical research and drug delivery<sup>3–5</sup>.

Because of the high pathogenic risk of the natural HA-producing strain *Streptococcus equi subsp. zooepidemicus*<sup>6</sup>, the development of non-pathogenic strains for heterologous HA production has received increasing interest. Many recombinant strains of *Escherichia coli*<sup>7</sup>,

<sup>1</sup>The Key Laboratory of Carbohydrate Chemistry and Biotechnology, Ministry of Education, School of Biotechnology, Jiangnan University, Wuxi, China. <sup>2</sup>The Science Center for Future Foods, Jiangnan University, Wuxi, China. <sup>3</sup>State Key Laboratory of Food Science and Resources, Jiangnan University, Wuxi, China.

<sup>4</sup>Jiangsu Province Basic Research Center for Synthetic Biology, Jiangnan University, Wuxi, China. <sup>5</sup>Institute of Future Food Technology, JITRI, Yixing, China.

<sup>6</sup>College of Environment and Energy, South China University of Technology, Guangzhou, China. ✉ e-mail: [zkang@jiangnan.edu.cn](mailto:zkang@jiangnan.edu.cn)

*Bacillus subtilis*<sup>8</sup>, *Lactococcus lactis*<sup>9</sup>, and *Pichia pastoris*<sup>10</sup> have been engineered as HA producers. In particular, *Corynebacterium glutamicum* is recognized as promising GRAS (generally recognized as safe) species for the industrial production of bio-based chemicals because of its flexible metabolism, high-stress resistance, and complete genome sequence data availability toolboxes for genome engineering and gene expression regulation<sup>11–13</sup>. *C. glutamicum* has been recently engineered as a robust HA cell factory by introducing hyaluronan synthase (HAS), strengthening the synthesis pathways for uridine diphosphate glucuronate (UDP-GlcA) and uridine diphosphate N-acetylglucosamine (UDP-GlcNAc), and weakening or blocking the competing pathways (e.g., lactate and exopolysaccharides)<sup>14–16</sup>. Although HA production has been increased using these approaches<sup>14,17</sup>, balancing HA biosynthesis and cell growth remains challenging, particularly under conditions of high viscosity and hypoxia. In addition, expanding the regulatory range of HA MW values is another critical issue.

The HASs responsible for catalyzing HA synthesis from UDP-GlcA and UDP-GlcNAc play vital roles in controlling HA MW<sup>18</sup>. Class I HAS enzymes are found in prokaryotes (such as Group A and C *Streptococci*), *Chlorella* viruses, and vertebrates. These enzymes are multifunctional membrane-bound proteins that couple HA polymerization and secretion. They differ in the directionality of chain elongation and are accordingly subdivided into two groups: Class I-R (reducing end addition; found in Group A and C *Streptococci*) and Class I-NR (non-reducing end addition; found in vertebrates and the *Paramesecium bursaria* *Chlorella* virus 1). Class II HAS is a cytoplasmic glycosyltransferase found only in *Pasteurella multocida* type A<sup>19–21</sup>. The determination of the topological structure of streptococcal HAS and the function of its different conserved regions<sup>22–29</sup> revealed that HAS activity depends on binding to phospholipids and is affected by factors such as fatty acid components, including carbon chain length and saturation level<sup>30–33</sup>. Recently, the first structure of a viral HAS was solved, and a model for substrate recognition, HA polymerization, and transport was established<sup>34</sup>, which provides insights into the function and molecular regulation mechanisms of HAS. The specific function of HAS domains has not yet been elucidated, and how HAS coordinately regulates HA polymerization, secretion, and MW also remains unclear. Thus, discovering the regulatory mechanism of HAS and constructing HAS mutants with higher capacities are significant and crucial for the biosynthesis of HA with controllable MWs.

In the present study, we reveal the crucial interplay between transmembrane helices (TMHs) and lipid composition in influencing HAS activity and cell shape. After elucidating the specific function of TMH-1 in HA export, we further highlight the critical role of hydrophobic interactions between residues 17 (TMH-1) and 45 (TMH-2) in facilitating this process. By systematically modifying TMH-1 and the intracellular catalytic domain, the engineered SzHAS variants achieve complete secretion of HA with MWs ranging from 300 to 1400 kDa. Then, upon discovering the inhibitory impact of increased UDP-glucuronic acid supply on cell division, we recover cell normal growth and rod shape by dynamically regulating UDP-glucose 6-dehydrogenase. Eventually, an adaptive laboratory evolution strategy was conducted to enhance the metabolic capacity of the engineered strains in high-viscosity conditions. The engineered strain *C. glutamicum* CGHA-125 produces 45 g L<sup>-1</sup> of HA in fed-batch cultures in 48 h. By controlling the activity of leech hyaluronidase (LHYal), we reduce broth viscosity and achieve an HA titer of 105 g L<sup>-1</sup>.

## Results

### Transmembrane regions and lipid composition are crucial for HA excretion

Class I HAS is a multifunctional transmembrane protein; its cytoplasmic domain is involved in substrate binding and HA

polymerization, while the transmembrane channel regulates HA elongation and excretion<sup>22</sup> (Fig. 1A). Based on the metabolic capacity to synthesize HA, *C. glutamicum* was selected as the chassis host. We then introduced *S. equi subsp. zooepidemicus* HAS (SzHAS) into *C. glutamicum* to synthesize HA and observed a surprising transformation in cell morphology, from the typical rod shape to an irregular shape (Fig. 1B and Supplementary Fig. S1). Transmission electron microscopy (TEM), phase contrast microscopy (PH), and scanning electron microscopy (SEM) revealed electron-transparent zones occupied by retained HA (Fig. 1B and Supplementary Fig. S1). Further analysis of HA by using high-performance liquid chromatography-mass spectrometry (HPLC-MS) and carbazole assay confirmed that all the produced HA was accumulated within *C. glutamicum* cells, rather than being secreted into the medium (Fig. 1C). These results confirmed that SzHAS retained its polymerization activity but was not able to transport HA out of the cell in *C. glutamicum* (Fig. 1D).

TEM images and propidium iodide staining results indicated severe cell membrane damage due to HA accumulation and interference (Fig. 1E and Supplementary Fig. S1). Simultaneously, cell growth and metabolism nearly stopped (Fig. 1F and Supplementary Fig. S2), and was accompanied by substantial alterations in global gene transcription (Supplementary Fig. S3 and Supplementary Data 1). To exclude potential effects derived from enzyme expression itself, we inactivated SzHAS by mutating the conserved catalytic motif DGS (residues 103–105) to AAA<sup>34</sup>. As expected, no similar effects were observed on cell growth, metabolism, morphology, or membrane environment were observed (Fig. 1F and Supplementary Fig. S2). The results confirmed that following the loss of the transportation function of SzHAS, accumulated HA disrupted cell membrane function (Fig. 1D and Supplementary Fig. S2) and severely impaired cell growth (Fig. 1F). The reason might be attributed to the abnormal conformation of the transmembrane channel of SzHAS in the recombinant *C. glutamicum* strain. Previous studies have shown that membrane lipid composition significantly influences the structure and function of membrane proteins by affecting protein-lipid interactions and modulating the physical properties of the cell membrane<sup>35–37</sup>. In this regard, we analyzed the lipid composition of the *C. glutamicum* cell membrane and found that the content of phosphatidylinositol (PI), in particular, was significantly lower in the *C. glutamicum* cell membrane than in *S. equi subsp. zooepidemicus* cell membrane (Fig. 1G and Supplementary Fig. S4). Consequently, we overexpressed PI synthase in *C. glutamicum* to increase PI synthesis (Fig. 1H, I and Supplementary Fig. S5). Despite the presence of HA in the cytosol, the growth of the recombinant *C. glutamicum* strain was partially restored (Fig. 1F), possibly due to the restoration of normal cell shape and membrane integrity (Fig. 1H and Supplementary Fig. S5). These findings underscore the critical role of the precise positioning and structural integrity of the SzHAS transmembrane channel in HA biosynthesis and export (Supplementary Fig. S5).

### The transmembrane helix TMH-1 controls extracellular transport of HA

In bacterial Class I-R HAS, four transmembrane helices (TMH-1–TMH-4) and three amphipathic interface helices (IF1–IF3) are conserved (Fig. 2A). Unlike SzHAS, *Streptococcus pyogenes* HAS (SpHAS) retains the ability to synthesize and transport HA in *C. glutamicum* (Supplementary Fig. S6)<sup>14</sup>, despite sharing a similar protein sequence and structure (Fig. 2A, B). To identify the pivotal region, we replaced each TMH and IF of SzHAS with the corresponding fragment from SpHAS. As shown in Figs. 2C, D, and Supplementary Fig. S7, only the mutant SzHAS<sup>SpTMH1</sup> restored HA transport capacity, thus suggesting that TMH-1 (residues 2–29) plays a crucial role in shaping the HA transport channel. To further validate this conclusion, we substituted TMH-1 (residues 2–29) of SpHAS with its counterpart from SzHAS and found that the mutant SpHAS<sup>SzTMH1</sup> lost the ability to transport HA but retained its ability to synthesize

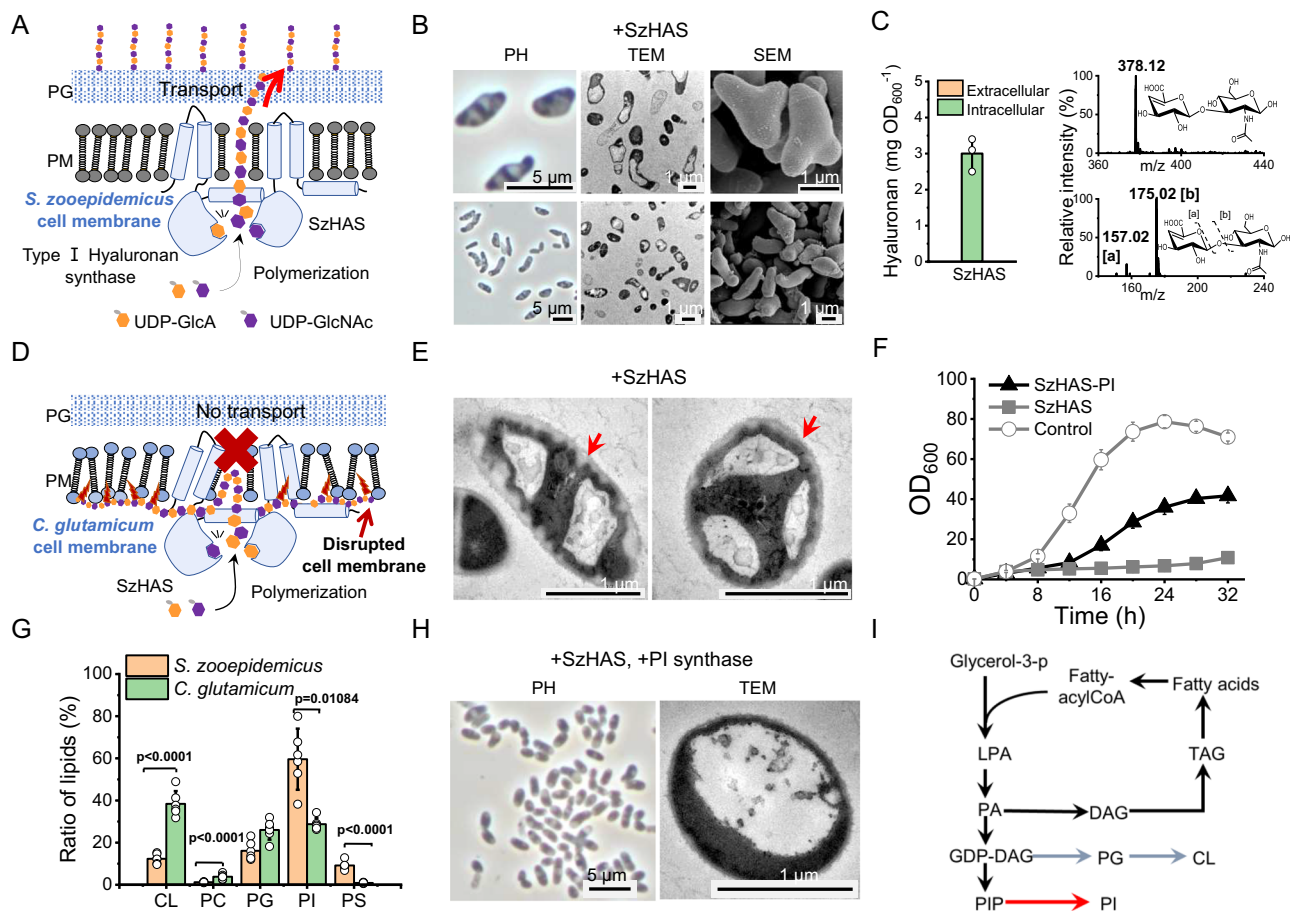


**Fig. 1 | HA accumulated in the cytosol of *C. glutamicum* expressing SzHAS derived from *S. equi subsp. zooepidemicus*.** **A** Schematics of Class I-R HAS. Class I-R HAS derived from *Streptococcus*, is a transmembrane protein that elongates and secretes HA. The cytosolic domain binds to activated nucleotide sugar monomers and facilitates glycosyltransferase reactions by alternately adding GlcA or GlcNAc to the growing HA chain. The HA chain elongates and translocates through the HAS pore, crossing the cell membrane until released. **B** PH, TEM, and SEM micrographs of *C. glutamicum* cells expressing SzHAS. PH microscopy observations were performed in triplicate and yielded similar results. **C** HA was detected in the cell pellets of *C. glutamicum*. Extracted ion chromatogram and mass spectra of HA analyzed by HPLC-MS. **D** Schematic showing HA accumulation in the cytosol and its effect on

cell membrane integrity. **E** TEM micrographs of *C. glutamicum* cells retaining HA. **F** Growth and metabolism curves of *C. glutamicum* cells expressing SzHAS and SzHAS mutants SzHAS<sup>103A-105A</sup> (lacking HA synthesis ability) as the control. SzHAS-PI overexpressed SzHAS and PI synthase. **G** Comparison of membrane lipid composition between *S. equi subsp. zooepidemicus* WSH-24 and *C. glutamicum* ATCC13032. Data are expressed as mean ± S.D. from six ( $n = 6$ ) independent biological replicates. **H** TEM micrographs of *C. glutamicum* cells expressing SzHAS and PI synthase. Cells cultivated for 32 h (late stationary phase). **I** Schematic diagram of the fatty acid synthesis of *C. glutamicum*. Statistical evaluation ( $p$ -value) was performed by a two-sided  $t$  test. The image shown is representative of  $n = 3$  independent replicates of experiments with similar results. Source data are provided as a Source Data file.

HA (Fig. 2E, F and Supplementary Fig. S7). Moreover, similar to SzHAS, SzHAS<sup>SpTMH-2</sup>, SzHAS<sup>SpTMH-4</sup>, SzHAS<sup>SpIF-1</sup>, SzHAS<sup>SpIF-2</sup>, SzHAS<sup>SpIF-3</sup>, and SpHAS<sup>SzTMH-1</sup> also showed impaired growth and metabolism (Fig. 2C and Supplementary Fig. S7). In contrast, the mutants SzHAS<sup>SpTMH-1</sup> (with secretion of HA, Fig. 2C) and SzHAS<sup>SpTMH-3</sup> (deficient in HA synthesis, Fig. 2C) restored cell growth and metabolism (Supplementary Fig. S7).

To investigate the effect of TMH-1 on HA transport, we used AlphaFold2<sup>38</sup> to simulate the three-dimensional structure of SzHAS. As shown in Fig. 2G, the transmembrane architecture consists of TMH-1 to TMH-4, resembling a tepee with helices straddling the cytosolic domain. TMH-1 is located in a groove between TMH-2 and TMH-4 and does not appear to directly participate in the formation of the HAS transmembrane channel (Fig. 2G and Supplementary Fig. S8). To elucidate the role of TMH-1, we deleted TMH-1 segments from SzHAS and SpHAS to generate the mutants SzHAS<sup>ΔTMH-1</sup> and SpHAS<sup>ΔTMH-1</sup>, respectively (Supplementary Fig. S8). Consistently, both mutants retained the ability to synthesize HA but lost their transport capabilities (Fig. 2H and Supplementary Fig. S8). The results confirmed that TMH-1 is involved in HA transport or secretion, but not synthesis. Moreover, a recent study by Maloney et al. identified a direct interaction between TMH-1

and TMH-2 in a viral HAS<sup>34</sup>. Therefore, we hypothesize that TMH-1 regulates the conformation of the HA transport channel by interacting with TMH-2 in SzHAS.

### Optimize transport channel for complete HA secretion and MW control

To identify the crucial residues responsible for controlling HA secretion, we systematically investigated residues 7–29, which form a transmembrane helix, and the N-terminal residues 2–6 located in the cytoplasm (Supplementary Fig. S8). The substitution residues 7–29 and residues 2–6 of SzHAS with the corresponding fragments from SpHAS, the mutants SzHAS<sup>Sp7T-29G</sup> and SzHAS<sup>Sp2P-6K</sup> achieved HA secretion (Fig. 3A). In contrast when residues 7–29 and residues 2–6 of SpHAS were replaced with the corresponding fragments from SzHAS, the resulting mutants SpHAS<sup>Sz7L-29G</sup> and SpHAS<sup>Sz2R-6N</sup> failed to secrete HA (Supplementary Fig. S9). The results of the local structural analysis suggest that replacement with segments 7T-29G or 2P-6K from SpHAS led to similar conformational changes in SzHAS<sup>Sp7T-29G</sup> and SzHAS<sup>Sp2P-6K</sup> (Fig. 3B). After further truncating the mutant region progressively, we found that only the mutation W17I enabled SzHAS to transport HA



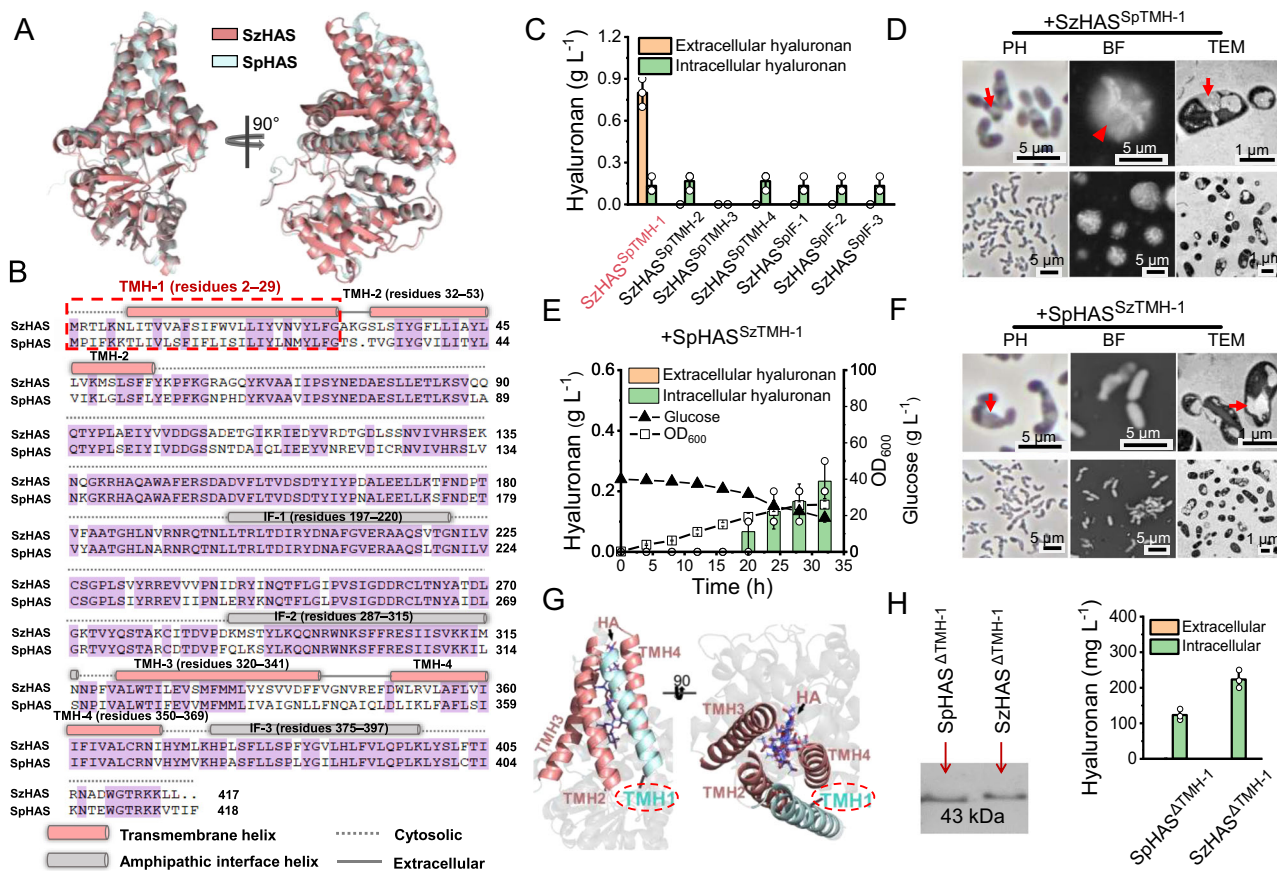


**Fig. 2 | TMH-I as a key region regulating the conformation of the HAS transmembrane channel. A, B** Comparative analysis of the tertiary structure and amino acid sequences between SpHAS and SzHAS. **C** Analysis of HA synthesis and transport in *C. glutamicum* expressing SzHAS mutants: SzHAS<sup>SpTMH-1</sup>, SzHAS<sup>SpTMH-2</sup>, SzHAS<sup>SpTMH-3</sup>, SzHAS<sup>SpTMH-4</sup>, SzHAS<sup>SpIF-1</sup>, SzHAS<sup>SpIF-2</sup>, and SzHAS<sup>SpIF-3</sup>. **D** PH, bright field (BF), and TEM micrographs of *C. glutamicum* cells expressing SzHAS<sup>SpTMH-1</sup>. **E** Growth curve, glucose consumption, and HA production of *C. glutamicum* expressing SpHAS mutant SpHAS<sup>SzTMH-1</sup>. **F** PH, BF, and TEM micrographs of *C.*

*glutamicum* cells expressing SpHAS<sup>SzTMH-1</sup>. **G** Protein structure of SzHAS predicted by AlphaFold2. **H** Western blotting (WB) analysis showing expression of HAS mutants SzHAS<sup>ΔTMH-1</sup> and SpHAS<sup>ΔTMH-1</sup>. HA synthesis by HAS mutants was analyzed in *C. glutamicum*. BF microscopy shows cells under BF after negative staining with 100 mg mL<sup>-1</sup> nigrosin for 5 min. All data presented as mean ± S.D. from three (*n* = 3) biological independent replicates. All microscopy experiments were performed in triplicate with similar results. Source data are provided as a Source Data file.

(Fig. 3C). By performing saturation mutagenesis of residue W17, we found that in addition to W17L, mutations of W17V, W17Q and W17L also facilitated HA transport (Fig. 3C and Supplementary Fig. S10). In particular, SzHAS<sup>W17L</sup> exhibited the highest transport capacity (Fig. 3C). The results revealed the crucial role of residue 17 in TMH-1 in regulating the conformation of the transmembrane channel. Four residues in TMH-2, L41, I42, L45, and L46, which are predicted to interact with 17 L (TMH-1), were individually mutated to alanine (Fig. 3C and Supplementary Fig. S10). SzHAS<sup>W17L/L45A</sup> alone lost HA transport ability, which confirmed the critical interaction between residues 17L (TMH-1) and L45 (TMH-2) in maintaining the appropriate channel for HA transport (Fig. 3B). Similarly, different N-terminal truncation mutants of SzHAS<sup>Sp2P-6K</sup> were constructed and compared to identify the critical residue (Fig. 3D). The residue at position 6 was determined to be crucial for HA transport (Fig. 3D, E). Western blotting (WB) assay revealed no differences in expression levels (Fig. 3F), thus negating any expression-related effects.

After identifying the critical residues for HA secretion, we focused on optimizing the transport channel to enhance HA transport efficiency. Saturation mutagenesis was performed on residue N6; the results showed that the mutation N6R yielded a higher extracellular HA titer (1.7 g L<sup>-1</sup>, Supplementary Fig. S11). Subsequently, the above-mentioned beneficial mutations were combined to generate SzHAS<sup>2P/3I/4F/6R/17L</sup> (Fig. 3G and Supplementary Fig. S11), which achieved complete secretion of HA with a titer of 1.9 g L<sup>-1</sup> in

flask cultures (Fig. 3H, I), 30% higher than that obtained from SpHAS<sup>14</sup>. Considering the effect of the interplay between the transport channel and HA nascent chain<sup>34</sup>, we determined HA MWs from different SzHAS variants. Remarkably, the MWs varied between 300 and 1400 kDa (Supplementary Figs. S12, S13, and Table 1). Moreover, when the HAS transport channel was in a “semi-open” state, the MW tended to be higher, for instance, SzHAS<sup>17Y</sup> (Supplementary Fig. S14). The reason might be attributed to the enhanced interaction between the semi-open HAS transport channel and HA, which promotes HA elongation and delays its release<sup>39</sup>.

### Engineer SzHAS catalytic region to enhance HA polymerization

Although Class I HAS enzymes show varying performance in *C. glutamicum*, their catalytic regions are highly conserved (Supplementary Fig. S15). To further improve HA polymerization capacity, the non-conserved sites Q89-Q90, A96, E108-T109, K112-R113, Q137, P179-T180, E236, D243, I246, K280, and I282 in the variant SzHAS<sup>2P/3I/4F/6R/17L</sup> were engineered (Fig. 4A and Supplementary Fig. S15). Compared to other mutations, the mutations of Q89V/Q90G, A96W, E108H/T109D, and D243K yielded enhanced HA production, resulting in yields of 2.5, 2.4, 2.4, and 2.5 g L<sup>-1</sup>, respectively (Fig. 4B–D and Supplementary Fig. S16). After combination, the variant SzHAS<sup>2P/3I/4F/6R/17L/89V/90G/96W/108H/109D/243K</sup> generated 2.9 g L<sup>-1</sup> of HA (300 kDa) (Fig. 4E and Supplementary Fig. S17), which was considerably higher than those achieved by SzHAS<sup>2P/3I/4F/6R/17L</sup> (1.9 g L<sup>-1</sup>) and SpHAS (1.5 g L<sup>-1</sup>)<sup>14</sup>.

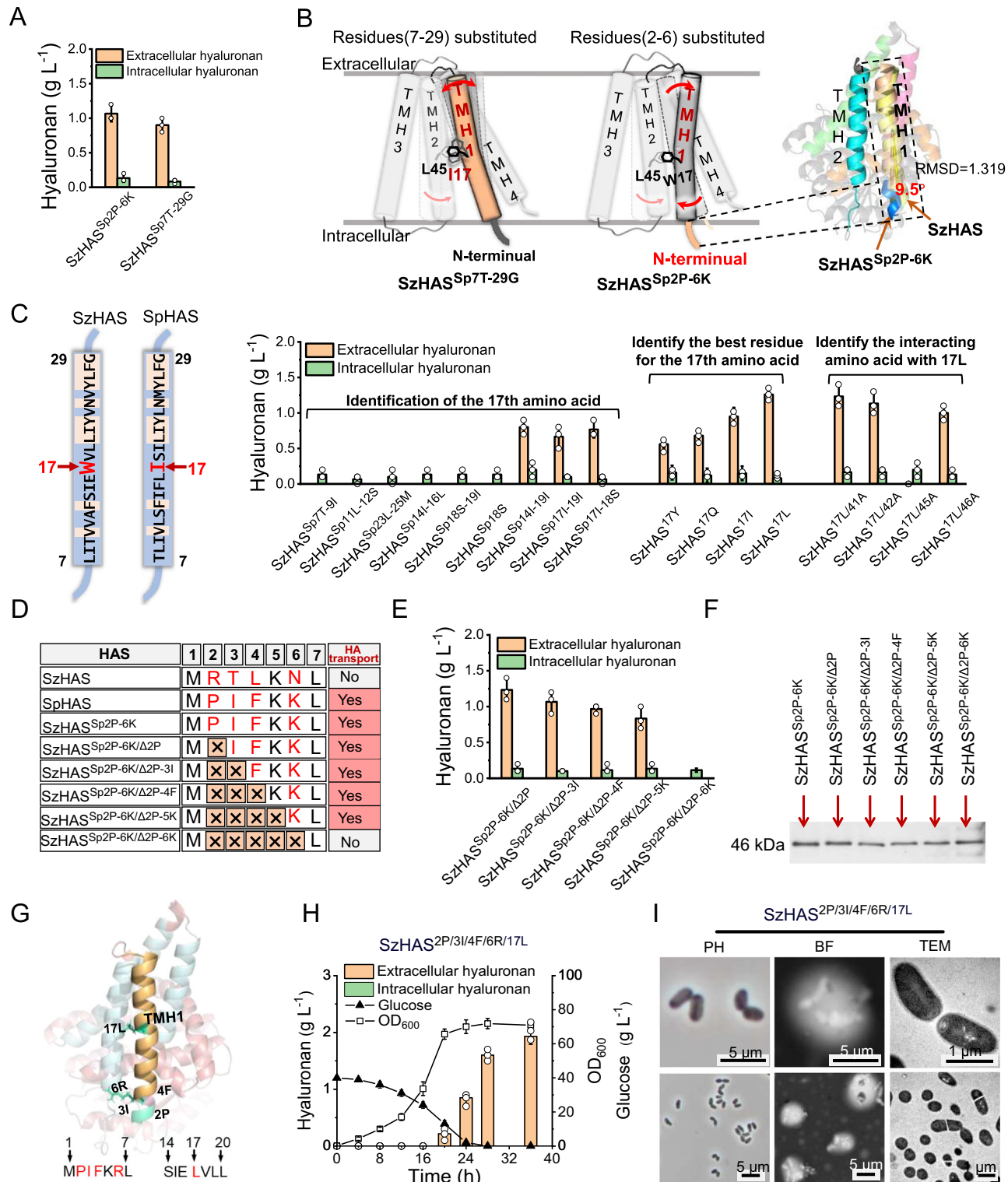


**Fig. 3 | Critical TMH1 region affecting HA transport.** **A** Analysis of HA synthesis by SzHAS mutants (SzHAS<sup>Sp2P-6K</sup>, and SzHAS<sup>Sp7T-29G</sup>). **B** Schematic showing residues (2–6) and (7–29) that affect the conformation of the HAS transport channel. AlphaFold2 predictions for the protein structure of SzHAS and SzHAS<sup>Sp2P-6K</sup> are presented. **C** Identification of key sites in the transmembrane region of TMH-1 affecting HA transport. Analysis of HA synthesis by SzHAS mutants (SzHAS<sup>Sp7T-9I</sup>, SzHAS<sup>Sp11L-12S</sup>, SzHAS<sup>Sp14I-19I</sup>, and SzHAS<sup>Sp23L-25M</sup>), (SzHAS<sup>Sp14L-16L</sup>, SzHAS<sup>Sp17I-19I</sup>, SzHAS<sup>Sp17I-18S</sup>, SzHAS<sup>Sp18S-19I</sup>, and SzHAS<sup>Sp18S</sup>), and (SzHAS<sup>17Y</sup>, SzHAS<sup>17Q</sup>, SzHAS<sup>17I</sup>, and SzHAS<sup>17L</sup>). **D–F** HA synthesis, transmembrane transport, and WB assay of N-terminal amino acid truncated mutants of SzHAS<sup>Sp2P-6K</sup> in *C. glutamicum*. **G** Modification of the HAS transmembrane region for highly efficient secretion of HA. **H** Growth, glucose consumption, and HA synthesis of *C. glutamicum* expressing SzHAS<sup>2P/3I/4F/6R/17L</sup>. **I** PH, BF, and TEM micrographs of *C. glutamicum* cells expressing SzHAS<sup>2P/3I/4F/6R/17L</sup>. Labels with × indicate the loss of an amino acid. All data are expressed as mean ± S.D. from three ( $n = 3$ ) independent biological replicates. Source data are provided as a Source Data file.

### Regulate UDP-GlcA synthesis to balance cell growth and HA production

Generally, the adequate supply of HA precursors UDP-GlcA and UDP-GlcNAc is crucial for HA biosynthesis (Fig. 5A). Hence, the specific enzymes UDP-glucose 6-dehydrogenase (encoded by *ugd*) and L-glutamine-D-fructose-6-phosphate aminotransferase (encoded by *glmS*) were overexpressed to increase the biosynthesis of UDP-GlcA and UDP-GlcNAc, respectively. Interestingly, we found that the morphology of *C. glutamicum* CGHA-105 cells (overexpressing SzHAS<sup>2P/3I/4F/6R/17L/89V/90G/96W/108H/109D/243K</sup>, *Ugd*, and *GlmS*) transformed to resemble that of *Streptococcus* strains (Fig. 5B and Supplementary Figs. S18 and S19). We confirmed that these morphological changes were due to the overexpression of *Ugd*, as *C. glutamicum* CGHA-107, which overexpresses *Ugd* alone, also exhibited the same morphological characteristics (Fig. 5C and Supplementary Fig. S19). This phenomenon was also observed in *B. subtilis* and the Gram-negative bacteria *E. coli* (Figs. 5D, S20–21). TEM of the sectioned cells revealed that chain formation is due to incomplete cell division (Fig. 5C). Moreover, despite no significant differences in protein expression levels (Fig. 5E and Supplementary Data 2), the appearance of the chain-rod-like morphology hindered cell growth and metabolism (Fig. 5F). This finding can be ascribed to the elevated content of

GlcA-containing polysaccharides in the cell wall (Fig. 5G), as it is well-known that the cell wall plays a crucial role in cell division<sup>40,41</sup>.

The recombinant *C. glutamicum* CGHA-105 strain begins HA synthesis during the mid-to-late growth phase, after 16 h, primarily between 20 and 32 h (Fig. 5J). However, began forming chain-rod-like morphology as early as 8 h (before HA synthesis starts) and maintained this morphology thereafter (Fig. 5B and Supplementary Fig. S19). This morphological change may be due to the misalignment between UDP-GlcA synthesis and HA synthesis. Therefore, the dynamic regulation of UDP-GlcA synthesis to optimize and harmonize both cell growth and HA synthesis seemed to be an attractive approach (Fig. 5H). For this purpose, we adopted a late exponential phase-responsive promoter P-N14 to guide *ugd* expression<sup>42</sup>. Although cell growth was restored, the production titer of HA significantly decreased (Supplementary Fig. S22), possibly due to the low transcriptional strength of promoter P-N14 (Fig. 5I). Accordingly, the non-conserved sequence of promoter P-N14 was mutated to generate strong promoters (Supplementary Fig. S22). The engineered promoter PH1 with 5-fold and 3-fold higher activity than those of P-N14 and *P<sub>trc</sub>*, respectively (Fig. 5I and Supplementary Fig. S22), was used for expressing *Ugd*. Consequently, the HA titer of the recombinant *C. glutamicum* CGHA-123 strain was increased to 10 g L<sup>-1</sup> (300 kDa), accompanied by enhanced cell density (OD<sub>600</sub>) and normal cell morphology in flask cultures (Fig. 5J, K).

**Table 1 | Weight average MWs of HA obtained from different hyaluronan synthases**

HAS	MW (kDa) <sup>a</sup>	PDI
SzHAS <sup>2P/3I/4F/6R/17L</sup>	300 ± 30	1.9 ± 0.3
SzHAS <sup>2P/3I/4F/6R</sup>	400 ± 20	1.5 ± 0.1
SzHAS <sup>2P/3I/4F/6A</sup>	500 ± 50	1.6 ± 0.3
SzHAS <sup>2P/3I/4F/6G</sup>	850 ± 60	1.1 ± 0.1
SzHAS <sup>7I</sup>	1200 ± 180	1.2 ± 0.2
SzHAS <sup>7Y</sup>	1400 ± 100	1.1 ± 0.1

<sup>a</sup>Data are expressed as mean ± SD from three (*n* = 3) biologically independent replicates. Source data are provided as a Source Data file.

### Adaptive laboratory evolution of CGHA-125 for high HA productivity

The biosynthesis capacity of the engineered *C. glutamicum* CGHA-123 was evaluated using a fed-batch cultivation process, and a final HA titer of 37 g L<sup>-1</sup> (500 kDa) was achieved at 48 h (Fig. 6A). However, after 36 h of culturing, the production of HA had already increased to 32 g L<sup>-1</sup>, which indicated a sharp decline in the ability of *C. glutamicum* CGHA-123 to synthesize HA between 36 and 48 h (Fig. 6A). This is because as the HA content increased, the solution became more viscous (Supplementary Movie 1), which limited the nutrient uptake and cell growth of the strain (Fig. 6B). Consequently, an adaptive laboratory evolution strategy with a high concentration of HA was applied to increase the

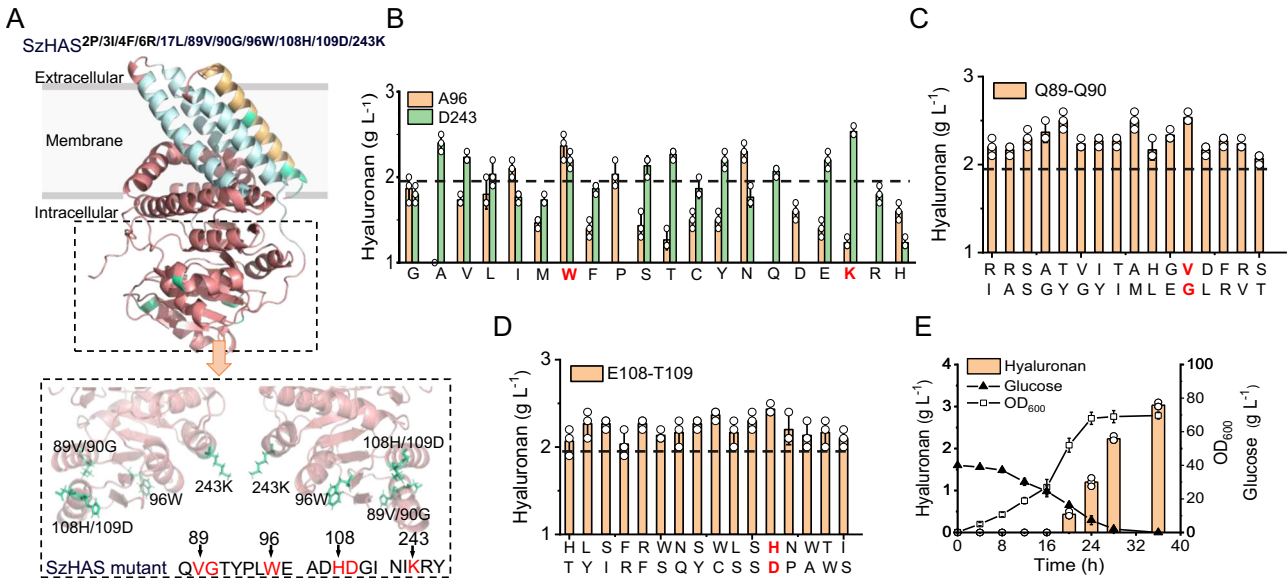


**Fig. 4 | Modification of the HAS catalytic region for highly efficient synthesis of HA.** **A** Protein structure of SzHAS<sup>2P/3I/4F/6R/17L/89V/90G/96W/108H/109D/243K</sup> predicted by AlphaFold2. **B–D** HA production by *C. glutamicum* strains with mutations at residues 89–90, 96, 108–109, and 243 of SzHAS<sup>2P/3I/4F/6R/17L</sup>. Residues Q89–Q90 and E108–T109 of the variant SzHAS<sup>2P/3I/4F/6R/17L</sup> were used to construct 200 engineered mutant

strains, and the mutant with the strongest HA synthesis ability was selected. **E** Growth, glucose consumption, and HA synthesis of *C. glutamicum* expressing SzHAS<sup>2P/3I/4F/6R/17L/89V/90G/96W/108H/109D/243K</sup>. All data are expressed as the mean ± S.D. from three (*n* = 3) independent biological replicates. Source data are provided as a Source Data file.



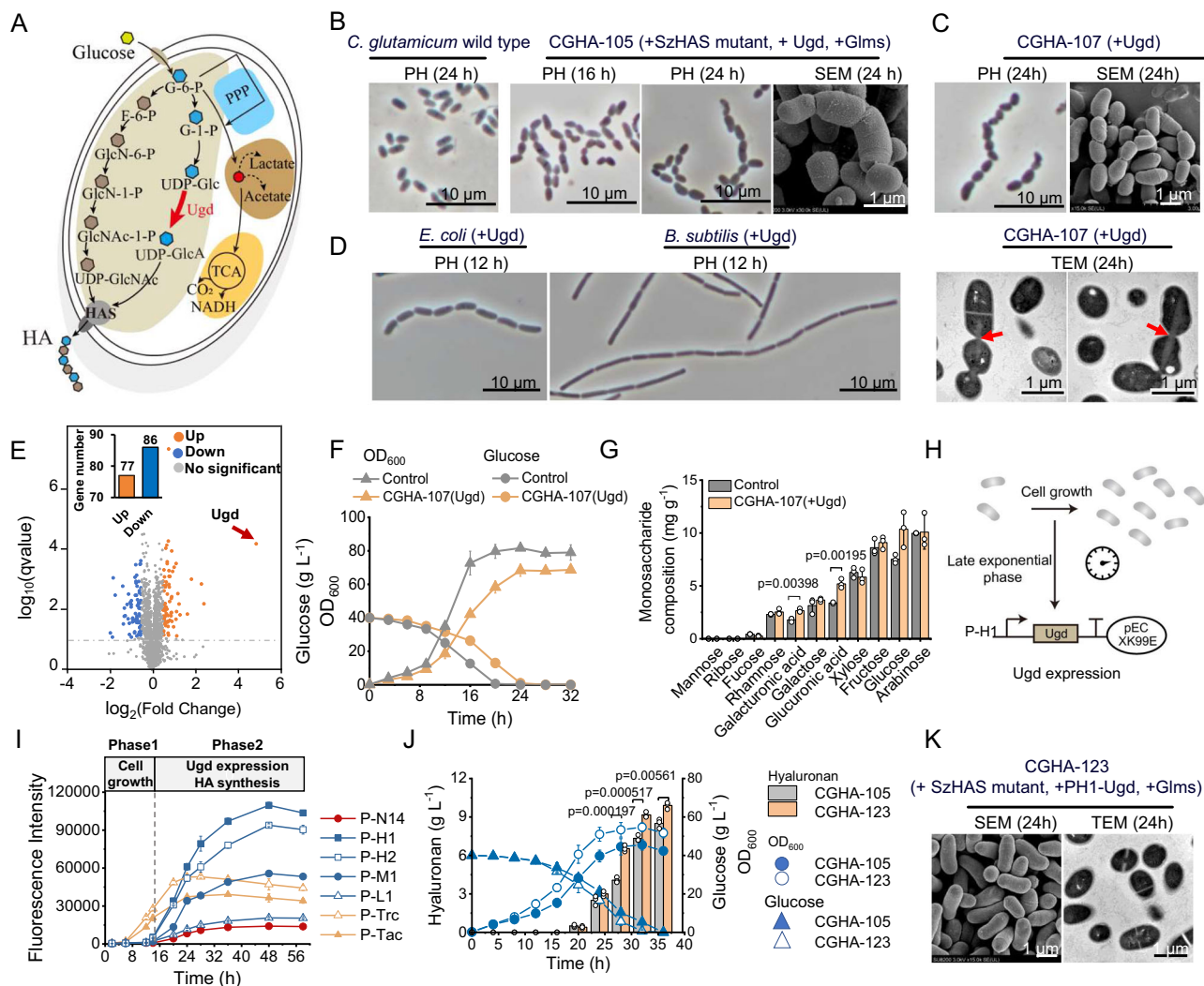


**Fig. 5 | Temporal control of UDP-GlcA synthesis for optimal cell growth and HA synthesis.** **A** The biosynthetic pathway for HA production from glucose. **B, C** PH, SEM, and TEM micrographs of the recombinant *C. glutamicum* CGHA-105 and CGHA-107 strains. **D** PH micrographs of recombinant *E. coli* and *B. subtilis* strains overexpressing UDP-glucose dehydrogenase (Ugd). **E** Volcano plot of differentially expressed proteins affected by changes in cell morphology. Orange and blue dots indicate up-regulation and down-regulation respectively. The abscissa represents the fold change in protein expression, while the ordinate represents significance changes in protein expression. **F** Growth and metabolism curves for *C. glutamicum* cells expressing Ugd and Ugd mutants (lacking catalytic activity). Ugd uses promoter P<sub>trc</sub>, while the mutant Ugd lacks catalytic activity, serving as a control. **G** Sugar composition of chain-like *C. glutamicum* cells determined using promoter P<sub>trc</sub> to overexpress Ugd, with *C. glutamicum* ATCC 13032 as control. **H** Temporal

regulation of Ugd expression balances cell growth and HA synthesis. Cells in the exponential phase, and late exponential phase show Ugd expression. **I** Expression of the *gfp* gene under promoter P-N14 and its derived promoters (P-H1, P-H2, P-M1, and P-L1) in wild-type *C. glutamicum*. **J** Growth and glucose consumption of the recombinant *C. glutamicum* CGHA-105 and CGHA-123. Strain CGHA-123 delays the expression of Ugd by promoter PH1. **K** SEM and TEM micrographs of the recombinant *C. glutamicum* strains CGHA-105 and CGHA-123, with promoter PH-1 used for Ugd expression. Cells were cultivated for 24 h and then subjected to proteomics sequencing and cellular polysaccharide composition analysis. Statistical evaluation (*p*-value) was performed by a two-sided *t* test. The image shown is representative of *n* = 3 independent replicates of experiments with similar results. All data are expressed as the mean ± S.D. from three (*n* = 3) biological independent replicates. Source data are provided as a Source Data file.

metabolic activity and robustness of *C. glutamicum* (Fig. 6B and Supplementary Fig. S23). Following 300 successive passages, the metabolic ability of the isolated strain *C. glutamicum* CGHA-125 was significantly improved (Fig. 6B) and 45 g L<sup>-1</sup> of HA with a MW of 500 kDa was produced in 48 h in a 5 L fermenter (Fig. 6A, and Supplementary Fig. S24). Genome resequencing revealed 85 genetic mutations (Supplementary Data 3). Transcriptome sequencing analysis showed that many genes involved in metabolic pathways were upregulated, particularly those associated with the energy biosynthesis pathways and stress resistance pathways were upregulated (Fig. 6C, D, Supplementary Fig. S23 and Supplementary Data 4), no changes were observed in the genes for the HAS enzyme or its UDP-sugar donor enzymes. For instance, the biosynthesis of lactic acid with the regeneration of NAD<sup>+</sup> from NADH was enhanced (Fig. 6D), which

was hypothesized to be advantageous in sustaining an increased metabolic rate under this high viscous and micro anaerobic conditions. To eliminate the capsule-like HA layer, increase glucose uptake<sup>14</sup> and produce low MW HA, 10,000 U mL<sup>-1</sup> LHyal, an HA degrading enzyme from Leech, was added to fed-batch cultures at 16 h. Consequently, following the consumption of 380 g L<sup>-1</sup> glucose, the titer, productivity, and conversion rate of low MW HA (10 kDa) reached 105 g L<sup>-1</sup>, 1.46 g L<sup>-1</sup> h<sup>-1</sup> and 27%, respectively (Fig. 6E and Supplementary Fig. S25), demonstrating the significant superiority of the engineered strain *C. glutamicum* CGHA-125 (Supplementary Table S1).

## Discussion

Although a three-dimensional structure of the HAS enzyme is lacking, different streptococcal HAS enzymes have been intensively

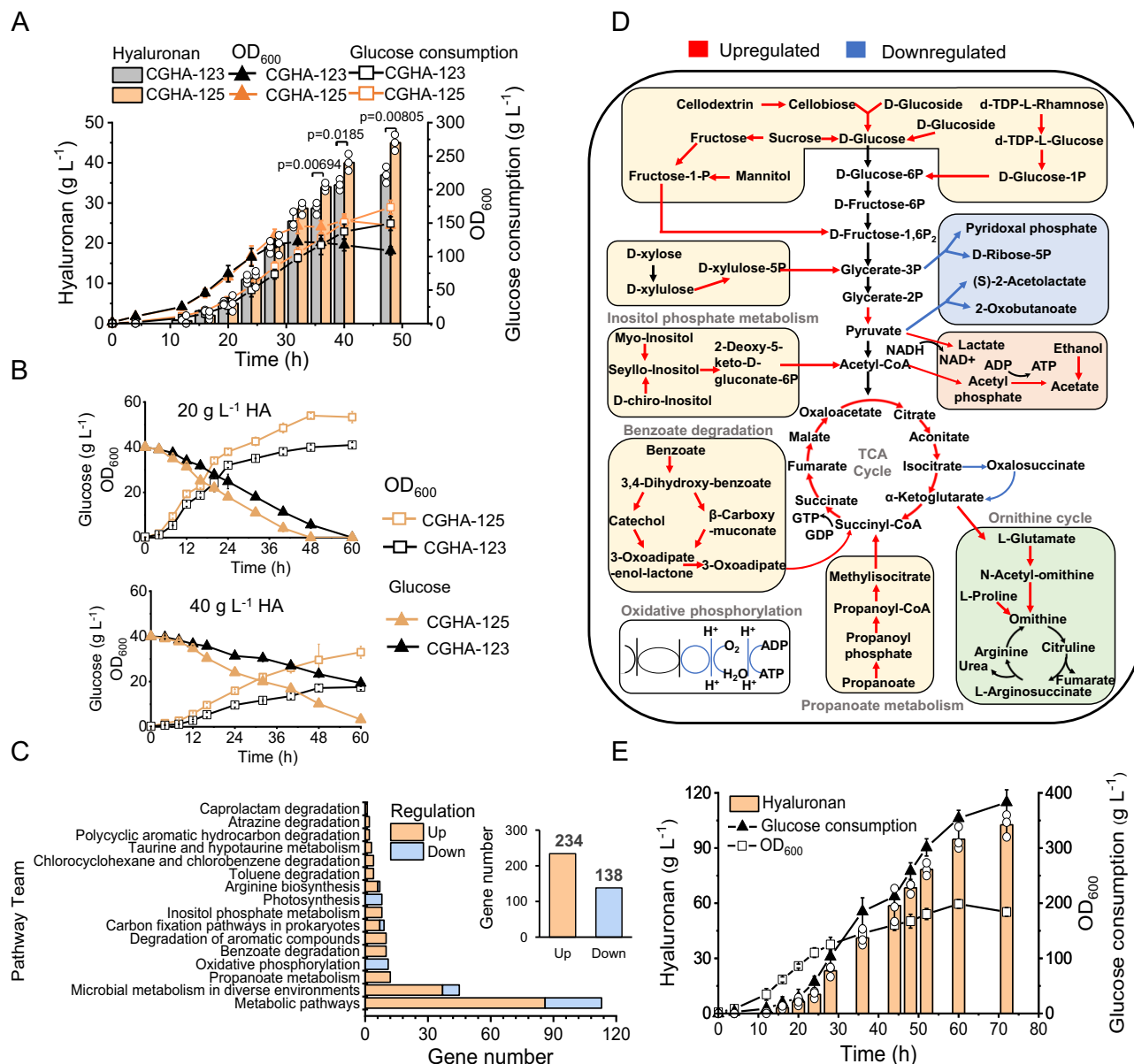


**Fig. 6 | Adaptive laboratory evolution improves the tolerance of *C. glutamicum* to viscous solution.** **A** Fed-batch cultivation of CGHA-123 and CGHA-125 in a 5-L fermenter. Real-time glucose consumption, cell density ( $OD_{600}$ ), and HA yield are plotted. **B** Effect of HA (MW 0.8–1 MDa) dissolved in culture broth on growth and glucose uptake by the CG-HA-Resistant strain, which adaptively evolved from *C. glutamicum* ATCC13032 in a high concentration HA solution. **C** Differential COG clusters indicating transcriptional differences between CG-HAT and wild-type *C. glutamicum*. The vertical axis shows COG classification, while the horizontal axis shows the number of differential genes. **D** Diagram of CG-HAT metabolism showing gene expression changes measured by transcriptomics analysis. Red and blue

arrows indicate upregulated and downregulated genes, respectively. Samples were collected at the 24 h time point (refer to B for cultivation details). **E** Fed-batch cultivation of *C. glutamicum* CGHA-125 in a 5-L fermenter. The culture was supplemented with L-Hyal hyaluronidase at the final concentration of 10,000 U mL<sup>-1</sup> at 16 h. Statistical evaluation ( $p$ -value) was performed by a two-sided  $t$  test. All data (excluding transcriptomics analysis) are expressed as mean  $\pm$  S.D. from three ( $n = 3$ ) independent biological replicates. Transcriptomics analysis data are expressed as mean  $\pm$  S.D. from two ( $n = 2$ ) independent biological replicates. Source data are provided as a Source Data file.

studied, and the topology<sup>22</sup> and several conserved residues of these enzymes for substrate binding<sup>18,24</sup> and HA chain initiation and polymerization have been tentatively identified or implicated in function<sup>27,43</sup>. In particular, the development of HA cell factories using different chassis cells and HAS enzymes revealed that different membrane environments severely affect the localization, conformation, and function of HAS<sup>31,32,34,44</sup>. Here, we found that SzHAS in *C. glutamicum* possesses only HA polymerization activity, but loses its capacity to transport the nascent sugar chain out of the cell, thereby resulting in abnormal cell morphology (Fig. 1B). An increase in PI content in *C. glutamicum* restored the cell shape and membrane

to their normal states even though HA was still present in the cytosol (Fig. 1H); this finding further confirmed the critical roles of protein-lipid interactions in regulating the structure and function of membrane protein<sup>44</sup>.

Recently, the cryo-electron microscopy structure of *Chlorella* virus HAS has been reported<sup>34</sup>, which guided us to simulate and compare the 3D structures of SzHAS and SpHAS. The conformation of TMH-1 in SzHAS and SpHAS shows a difference (Fig. 2A), thus suggesting its important role in maintaining a continuous transmembrane channel for HA secretion. In fact, we found that TMH-1, as a disordered sequence is located in the groove between TMH-2 and TMH-4 and does



not directly contribute to HA transport channel formation<sup>34</sup> (Fig. 2G). Truncated analysis of different HAS TMH-1 sequences revealed that TMH-1 is involved in HA transport but not in HA synthesis (Fig. 2H). The results of structure-assisted saturated mutation and computational alanine scanning further confirmed that the interaction between residues 17 (TMH-1) and 45 (TMH-2) (Fig. 3B, C) plays a decisive role in regulating the conformation of the transport channel. Interestingly, we found that residue Lys<sup>6</sup> in the intracellular N-terminal fragment also contributes to the correct location and conformation of TMH-1 (Fig. 3B, D). After integrating all the positive mutations, the variant SzHAS<sup>2P/3I/4F/6R/17L</sup> exhibited higher polymerization and transport capacity than SpHAS<sup>14</sup> and achieved the complete secretory synthesis of HA (Fig. 3H, I). These findings indicate that modulation of the conformation of specific transportation channels by altering local sequences is an effective strategy for optimizing transmembrane protein-dependent catalytic synthesis. The results also confirmed the influence of the HA translocation channel on the control of HA MW (300–1400 kDa, Table 1). Recently, Baggenstoss et al. identified a highly conserved B-X7-B motif (K398-X7-R406-X7-K414) that participates in the control of HA synthesis activity and MW in *Streptococcus equisimilis* HAS (SeHAS)<sup>43</sup>. By performing site-directed mutation of Lys<sup>398</sup>, HA of smaller size ( $\leq 250$  kDa–480 kDa) was generated with the extracted membranes containing SeHAS<sup>43</sup>. Almost at the same time, Jiang et al. also demonstrated the key role of the C-terminus of SeHAS in HA synthesis and MW control. By performing site-directed mutation of residues K414–417, the HA size was increased with a higher binding affinity between SeHAS C-terminus and the HA chain<sup>27</sup>. Taken together with our work, it seems promising to produce HA with a specific degree of polymerization by remodeling the HAS transport channel and the C-terminal motif. In 2007, before 3-D structures, accurate computer predictions, and extensive mutagenesis data were available for the class I HAS members, it was hypothesized that the HA chain/HAS enzyme interaction strength could be a means to modulate the polymer size<sup>45</sup>. Here, our data supports this general concept.

Although traditional metabolic engineering strategies have been used to construct microbial cell factories of interest, issues such as unexpected metabolic imbalances and irregular cell growth persistently occur<sup>46–49</sup>. Here, we found that the morphology of *E. coli*, *B. subtilis*, and *C. glutamicum* cells changed into the chain-rod shape with an undivided cell wall following the enhanced supply of UDP-GlcA (Fig. 5B–D); this finding further confirmed the essential role of the biosynthesis and hydrolysis of cell wall polysaccharides in cell division<sup>50</sup>. Regarding the balance of UDP-GlcA synthesis toward cell growth and HA production (Fig. 5H), strong late exponential phase promoters were engineered and used for modulating the expression of *ugd* (Fig. 5I). The recovered normal state of cell shape and cell growth, and the increased HA titer (Fig. 5J, K) demonstrated the efficacy of this dynamic regulation strategy.

*C. glutamicum* is a strictly aerobic bacterium. The cell metabolism activity decreases under highly viscous conditions because of the restricted uptake of nutrients, including glucose and oxygen<sup>14</sup>. Here, we developed an adaptive evolutionary strategy and successfully improved the metabolic capacity of the recombinant *C. glutamicum* CGHA-125 strain under micro anaerobic conditions (Fig. 6A, B). Transcriptome data analysis showed that the evolved *C. glutamicum* CGHA-125 strain exhibited an upregulated flux toward lactate and acetate and a downregulated TCA (tricarboxylic acid) cycle (Fig. 6C, D). Moreover, following the addition of corn steep liquor, the metabolic pathways of other sugars and the reaction toward succinate were also upregulated. In this case, the accelerated production of GTP and the regeneration of NAD<sup>+</sup> led to a higher glucose consumption rate and amount (Fig. 6D). More recently, to decrease carbon dissipation and facilitate chemical biosynthesis, Zhou et al. used an adaptive laboratory evolution strategy and engineered a TCA cycle-deficient *E. coli* strain as an efficient chassis host for biotechnological applications<sup>51</sup>. Thus, the results

highlight the effectiveness of the adaptive evolution approach, particularly in enhancing strain properties, for producing highly viscous compounds.

In conclusion, by systematically studying and reconstructing SzHAS, balancing HA biosynthesis and cell growth, and improving the metabolic capacity of the engineered *C. glutamicum* strain under high viscosity conditions, we achieved the complete secretory biosynthesis of HA with a broader MW control range. The titer, productivity, and conversion rate of high MW HA (500 kDa) and low MW HA (10 kDa) reached 45 and 105 g L<sup>-1</sup>, 0.94 and 1.46 g L<sup>-1</sup> h<sup>-1</sup>, and 33% and 27%, respectively (Supplementary Table S1). The results not only advance our understanding of HAS structure and function and the mutual influence between cell metabolism and cell morphology, but they also offer valuable insights into the biosynthesis of polysaccharides. This study also provides a shape-guided engineering strategy to optimize microbial cell factories.

## Methods

### Strains, plasmids, and reagents

The bacterial plasmids and strains used in this study are listed in Supplementary Data 5 and Supplementary Data 6, respectively. *E. coli* Top 10 was used for plasmid cloning and propagation, and *C. glutamicum* ATCC 13032 was used as the chassis host for constructing HA-producing strains. Plasmids pXMJ19 and pECXK99E were used for gene expression. The *szHAS*, *spHAS*, *gfp* genes were codon-optimized and synthesized by GENEWIZ (Suzhou, China). The *ugd* gene was amplified from the *C. glutamicum* genome. The sequences and associated accession numbers are provided in Source Data. All chemicals and kits were purchased from Sangon Biotech (Shanghai, China) unless specifically mentioned. PrimeStar DNA polymerase, Ex Taq<sup>®</sup> DNA polymerase, and all restriction enzymes were purchased from Takara (Dalian, China).

### Strain cultivation and shake-flask fermentation

The strains used in this study are listed in Supplementary Data 7. *E. coli* Top 10 cells were cultured in Luria-Bertani (LB) medium supplemented with 50  $\mu$ g mL<sup>-1</sup> kanamycin or chloramphenicol when necessary. *C. glutamicum* strains were routinely cultivated at 30 °C in BHIS medium [37 g L<sup>-1</sup> Brain Heart Infusion (Difco), 91 g L<sup>-1</sup> sorbitol]<sup>50–52</sup>. The antibiotics kanamycin (25  $\mu$ g mL<sup>-1</sup>) and chloramphenicol (15  $\mu$ g mL<sup>-1</sup>) were added when necessary.

All flask-scale cell cultures were performed using 250 mL flasks containing 25 mL of a modified minimal medium. The *C. glutamicum* shake flasks medium (glucose-corn steep medium)<sup>14</sup> consisted of 42 g L<sup>-1</sup> MOPS [3-(N-morpholino) propane sulfonic acid], 20 g L<sup>-1</sup> corn steep powder, 20 g L<sup>-1</sup> (NH<sub>4</sub>)<sub>2</sub>SO<sub>4</sub>, 0.25 g L<sup>-1</sup> MgSO<sub>4</sub>, 1 g L<sup>-1</sup> K<sub>2</sub>HPO<sub>4</sub>, 1 g L<sup>-1</sup> KH<sub>2</sub>PO<sub>4</sub> supplemented with 40 g L<sup>-1</sup> glucose, at pH 7.0. Iso-propyl- $\beta$ -D-thiogalactoside (IPTG, 0.25 mM) was added to induce target gene expression. All shake-flask fermentation experiments were performed with three biologically independent replicates ( $n = 3$ ), and analyses were conducted once for each growth condition.

### Plasmid cloning and site-directed mutagenesis

All primers used in this study were synthesized by GENEWIZ, and listed in Supplementary Data 7. Site-directed mutations were performed as follows: Overlapping primers were designed to amplify the plasmid containing mutated genes. The plasmid was amplified with PCR, and 5  $\mu$ L of the mixture was transformed into 50  $\mu$ L of *E. coli* competent cells through heat-shock transformation. All mutations were verified by sequencing.

### Measurement of cell growth and metabolite concentration

The cell concentration was determined by measuring the OD<sub>600</sub> value with a spectrophotometer (Shimadzu, Shanghai, China). The residual glucose levels were quantified using a glucose analyzer (Shenzhen Siemantec Technology, Shenzhen, China). HA was purified as follows:

extracellular HA was purified by three rounds of ethanol precipitation, while intracellular HA was first obtained through cell lysis at high temperatures and then purified through multiple rounds of ethanol purification<sup>28</sup>. The concentration of HA in the purified samples was assessed by carbazole assay<sup>53</sup>. D-glucuronic acid was used as an external standard, and *C. glutamicum* carrying the blank vector served as the negative control. All cell growth and metabolite concentration measurements were performed with three biologically independent replicates ( $n=3$ ), and analyses were conducted once for each growth condition.

#### WB assay

*C. glutamicum* cells were collected by centrifugation and treated with 20 mg L<sup>-1</sup> lysozyme at 37 °C for 2 h to degrade the cell wall. The cells were then lysed by sonication in a buffer containing 50 mM Tris-HCl, 1 mM phenylmethanesulfonyl fluoride, and 5 mM ethylenediaminetetraacetic acid. Following the BCA protein concentration assay, equal amounts of total protein samples were subjected to SDS-PAGE. Subsequently, WB assay was performed using YTHXBio ZA004 His-tag mouse monoclonal antibodies and horseradish peroxidase-labeled YTHXBio ZM03 goat anti-mouse IgG (H + L)-HRP (YTHX Biotechnology, Beijing, China).

#### Ultra-thin section TEM analysis

TEM imaging was performed with a Hitachi H7650 transmission electron microscope (Tokyo, Japan) at 80 kV. Cells were collected by centrifugation, washed three times with a glutaraldehyde solution (5% (v/v) glutaraldehyde, 0.1 M PBS; pH 7.2), and then washed three times with an OsO<sub>4</sub> solution (1% (v/v) OsO<sub>4</sub>, 0.1 M PBS; pH 7.2). The samples were dehydrated through a graded series of ethanol [30, 50, 70%, and 90% (v/v)] and then thoroughly rinsed three times with pure ethanol. Next, the cells were processed for embedding (Sigma-Aldrich EPON 812, Shanghai, China), sectioning (Leica EM UC7; Leica, Wetzlar, Germany), and staining with lead citrate. The stained specimens were then examined under TEM for further analysis.

#### Cold-field emission SEM analysis

SEM imaging was performed with a cold-field emission scanning electron microscope (Hitachi SU8220; Tokyo, Japan). Cells were washed three times with a glutaraldehyde solution (5% (v/v) glutaraldehyde, 0.1 M PBS; pH 7.2) at 4 °C and then washed three times with a PBS solution (0.1 M PBS; pH 7.2). The samples dehydrated through a graded series of ethanol [30, 50, 70, and 90% (v/v)] and then thoroughly rinsed three times with pure ethanol. Next, the cells were processed for drying (Leica CPD-300, Leica, Wetzlar, Germany), and sputtering (Leica ACE-600; Leica), and then examined by cold-field emission SEM for further analysis.

#### Protein structure simulation and comparison

Structural models of SzHAS, SpHAS, and SzHAS and SpHAS mutants were generated using AlphaFold2<sup>38</sup> and RoseTTAfold<sup>54</sup>. The open-source version of PyMol was used for structural comparison, 3D structure visualization, and structural analysis.

#### Analysis of cell morphology by microscopy

To perform Propidium Iodide staining, the cells were harvested by centrifugation and washed three times with PBS to remove any residual contaminants. The cells were then incubated with a Propidium Iodide solution (0.5 mg mL<sup>-1</sup>) at room temperature for 15 min and observed under a microscope (Nikon Eclipse Ni-E microscope, Tokyo, Japan) to evaluate the staining results. To visualize lipid localization, the cells were washed three times with PBS, and a 1% (v/v) Nile Red [9-diethylamino-5H-benzo (α) phenoxa-phenoxazine-5-one] solution

(0.1 mg mL<sup>-1</sup> in acetone) was added, followed by incubation in the dark for 10 min. Finally, the cells were examined using a fluorescence microscope to detect Nile Red fluorescence. Micrographs were processed with ImageJ software (National Institutes of Health, Bethesda, MD, USA)<sup>55</sup>. All microscopy analyses were performed using three biologically independent replicates ( $n=3$ ), with each growth condition analyzed once.

#### Measurement of weight-average MW of HA

High-performance size-exclusion chromatography (HPSEC) multi-angle laser light scattering (MALLS) was used to measure the weight average MW of HA. A 200 μL purified HA sample was analyzed with an HPSEC-MALLS system comprising a Waters 515 HPLC pump, Shodex OHPak SB-806HQ and SB-804HQ column series, a DAWN HELEOS II MALLS detector, and an Optilab dRI detector. An injection volume of 100 μL was used, and the dn/dc constant for MALLS was 0.138. The HA sample was separated into fractions using a mobile phase of 0.1 M NaNO<sub>3</sub>, and 0.02% (m/v) NaN<sub>3</sub> at 40 °C and a flow rate of 0.5 mL min<sup>-1</sup>. All HA weight average MW measurements were performed with three biologically independent replicates ( $n=3$ ), and analyses were conducted once for each growth condition. The final weight average MW of the HA was determined by averaging the results of measurements of three separate biologically independent replicates.

#### Cell membrane lipid omics analysis

Ultra-high-performance liquid chromatography-mass spectrometry (UHPLC-MS) was conducted for analyzing cell membrane lipid omics. First, a sample of 30 ± 3 mg was accurately weighed. Next, 200 μL deionized water, 20 μL internal lipid standard mixture, 800 μL methyl tert-butyl ether, and 240 μL precooled methanol were sequentially added to the sample. The mixture was then placed in a low-temperature water bath and sonicated for 20 min to promote extraction efficiency. Subsequently, the sample was allowed to stand at room temperature for 30 min to ensure thorough mixing. Finally, the mixture was centrifuged, and the upper organic phase was collected. The treated sample was then dried under a stream of nitrogen gas. The dried sample was dissolved in 200 μL of a 90% isopropanol/acetonitrile solution and centrifuged again to obtain the supernatant for subsequent UHPLC analysis.

The UHPLC Nexera LC-30A system, equipped with a C18 reverse-phase chromatographic column (column temperature: 45 °C), was used for sample separation at a flow rate of 300 μL min<sup>-1</sup>. The mobile phase consisted of two components: Component A was a mixture of 60% acetonitrile and 40% water; Component B was a mixture of 10% acetonitrile and 90% isopropanol. The gradient elution program was set as follows: 0–2 min, Component B proportion was maintained at 30%; 2–25 min, Component B proportion was increased linearly to 100%; 25–35 min, Component B proportion was returned to 30% to balance the chromatographic column. The sample temperature in the autosampler was kept at 10 °C throughout the analysis.

After UHPLC separation, the samples were subjected to MS by using a Q Exactive series mass spectrometer. The electrospray ionization technique was used for detection in both positive and negative ion modes. The instrument parameters were as follows: heater temperature, 300 °C; sheath gas flow rate, 45 arb; auxiliary gas flow rate, 15 arb; sweep gas flow rate, 1 arb; spray voltage, 3.0 kV; capillary temperature, 350 °C; S-Lens RF level, 50%; and MS1 scan range, 200–1800 m/z. Under these conditions, the UHPLC-MS analysis effectively achieved qualitative and quantitative analysis of the target compounds. All cell membrane lipid omics analysis measurements were performed with six biologically independent replicates ( $n=6$ ), and analyses were conducted once for each growth condition.

### Analysis of polysaccharide constituents of *C. glutamicum*

*C. glutamicum* and the engineered strain were cultivated in a culture medium at 30 °C for 24 h. The culture medium was centrifuged at  $7155 \times g$  for 20 min and the supernatants were discarded. The cells were washed three times with PBS, harvested by centrifugation, and then freeze-dried. Cell samples were weighed and hydrolyzed with trifluoroacetic acid at 121 °C for 2 h. The samples were blow-dried under nitrogen. Next, the samples were washed with 99.99% methanol, blow-dried again, and repeatedly washed with methanol for 2–3 times. Sugar constituents were quantified using a Thermo ICS5000 ion chromatography system equipped with a Dionex™ CarboPac™ PA20 column ( $150 \times 3.0$  mm,  $10 \mu\text{m}$ ). The mobile phases comprised: mobile phase A ( $\text{H}_2\text{O}$ ), mobile phase B (0.1 M NaOH), and mobile phase C (0.1 M NaOH, 0.2 M NaAc), flow rate 0.5 mL/min. The column temperature was 30 °C and the injection volume was  $5 \mu\text{L}$ . All polysaccharide constituent measurements were performed with three biologically independent replicates ( $n=3$ ), and analyses were conducted once for each growth condition.

### Transcriptomics and proteomics analyses

For transcriptomics and proteomics analyses, engineered *C. glutamicum* strains were cultivated at 30 °C and 200 rpm in the glucose-corn steep medium. Cells were incubated at 30 °C for 24 h and collected by centrifugation at 4 °C, and the pelleted cells were rapidly frozen in liquid nitrogen. Transcriptome and proteomics sequencing was performed by GENEWIZ. After removing the sequencing adapters and trimming consecutive low-quality bases (quality < 20) from the reads, high-quality RNA-sequencing reads were aligned, and gene expression abundance was quantified by fragments per kilobase of exon per million fragments mapped. Total RNA was extracted using TRIzol or RNeasy Mini Kit (Qiagen), and its quality checked with Agilent 2100/2200 Bioanalyzer, NanoDrop, and agarose gel. One microgram of RNA underwent rRNA depletion, fragmentation, and reverse transcription into cDNA using ProtoScript II Reverse Transcriptase. Second-strand cDNA synthesis used a mix including dACGTP/dUTP. After end repair and dA-tailing, adapters were ligated, and size selection recovered ~400 bp fragments. The dUTP-marked second strand was digested. Libraries were PCR-amplified with P5/P7 primers for flow cell bridge PCR and multiplexing, cleaned with beads, validated by Qsep100, and quantified by Qubit 3.0.

Proteins were extracted using SDT buffer (4% SDS, 100 mM Tris-HCl, 1 mM DTT, pH 7.6) and quantified with the BCA Protein Assay Kit (Bio-Rad, USA). Following the FASP procedure, proteins were digested with trypsin, peptides desalted on C18 cartridges, concentrated by vacuum centrifugation, and reconstituted in 0.1% formic acid. Each sample (200  $\mu\text{g}$  protein) was mixed with SDT buffer, detergents, and low-molecular-weight components removed using UA buffer (8 M urea, 150 mM Tris-HCl, pH 8.0) via ultrafiltration, and cysteine residues blocked with iodoacetamide. After washing, samples were digested overnight with trypsin. For SDS-PAGE, 20  $\mu\text{g}$  protein per sample was boiled, separated on a 12.5% gel, and visualized by Coomassie Blue staining. TMT labeling used 100  $\mu\text{g}$  peptide mixture per sample, fractionated into 10 fractions using a High pH Reversed-Phase Kit (Thermo Scientific). LC-MS/MS analysis was performed on a Q Exactive mass spectrometer for 60 or 90 minutes using a data-dependent top10 method. MS raw data were analyzed using Mascot within Proteome Discoverer 1.4, followed by comprehensive bioinformatic analyses including hierarchical clustering, subcellular localization, domain annotation, GO and KEGG pathway mapping, enrichment, and protein-protein interaction analysis.

The whole transcriptome and proteomics results can be found in Supplementary Data. Transcriptomics measurements were performed using two biologically independent replicates ( $n=2$ ), proteomics analyses were performed using three biologically independent replicates ( $n=3$ ), and analyses were conducted once for each growth condition.

### Genomic re-sequencing

Genomic re-sequencing on Illumina HiSeq/Novaseq/MGI2000 platforms followed the manufacturer's protocol. DNA (200  $\mu\text{g}$ ) was fragmented to 300–350 bp, end-repaired, and adapter-ligated. Size selection used Cleanup beads, then 8 PCR cycles added flowcell-compatible sequences and a six-base index. PCR products were validated with an Agilent 2100 Bioanalyzer. Libraries were sequenced PE150. Data analysis removed adaptors, PCR primers, N bases > 14, and Q20 < 40% using fastp (V0.23.0). Sentieon (V202112.02) mapped reads, removed duplicates and called SNVs/InDels. Annovar annotated SNVs/InDels, while breakdancer and CNVnator analyzed structural variations. The whole genomic re-sequencing results can be found in Supplementary Data.

### HA quantification using HPLC-MS

Complete depolymerization of HA was achieved using hyaluronanase. The sample was mixed with nine volumes of methanol, then centrifuged at  $16,000 \times g$  for 20 min to collect the supernatant, which was subsequently filtered through a  $0.22 \mu\text{m}$  membrane filter (ALWSCI, Shaoxing, China). The filtrate was analyzed using an LC-IT-TOF-MS system (Shimadzu, Kyoto, Japan) equipped with a  $5 \mu\text{m}$  Shim-pack VP-ODS column ( $4.6 \times 250$  mm) maintained at 40 °C. For elution, Buffer A consisted of ultra-pure water and Buffer B was a methanol solution, both containing 8 mM ammonium acetate. The LC gradient elution program was as follows: from 0 to 5 min, 5% Buffer B; from 5 to 15 min, a linear gradient from 5% to 60% Buffer B; and from 15 to 20 min, 60% Buffer B, with a flow rate of 0.2 mL/min. The LC effluent was ionized using an electrospray ionization source operated at 2 kV and 230 °C, with nitrogen serving as both the drying and nebulizing gas. Negative ion spectra were acquired by scanning the mass-to-charge ratio ( $m/z$ ) range from 100 to 900.

### Statistics and reproducibility

Statistical analysis was performed using Microsoft Excel (2019) and Origin Pro (2019b). Graphed data are represented as the mean  $\pm$  standard deviation (mean  $\pm$  s.d.). A Two-tailed Student's  $t$  test was used to compare the differences between the two groups, with a significance level set at  $P < 0.05$ . Randomized sampling was employed for the analysis of all microbial samples. For the HA MW determination, HA titer measurement, cell morphology observation experiments, cell growth and metabolism curve test, cell polysaccharide constituents analysis, proteomics analysis, lipid omics analysis, at least three independent growths were conducted, and analyses were performed once for each growth. In transcriptomic analysis, two independent growths were conducted, and analyses were performed once for each growth.

### Reporting summary

Further information on research design is available in the Nature Portfolio Reporting Summary linked to this article.

### Data availability

The genomics and transcriptomics raw files are available at the Genome Sequence Archive under accession code [CRA022690](#). The proteomics and lipidomics raw files are available at OMIX with OMIX IDs [OMIX008904](#) and [OMIX008905](#). All data are available in the main text or the Supplementary Information/Source Data file. Source data are provided in this paper.

### References

- Kang, Z., Zhou, Z., Wang, Y., Huang, H., Du, G. & Chen, J. Bio-based strategies for producing glycosaminoglycans and their oligosaccharides. *Trends Biotechnol.* **36**, 806–818 (2018).
- Kobayashi, T., Chanmee, T. & Itano, N. Hyaluronan: metabolism and function. *Biomolecules* **10**, 1525 (2020).



3. Snetkov, P., Zakharova, K., Morozkina, S., Olekhovich, R. & Uspenskaya, M. Hyaluronic acid: the influence of molecular weight on structural, physical, physico-chemical, and degradable properties of biopolymer. *Polymers* **12**, 1800 (2020).
4. Sze, J. H., Brownlie, J. C. & Love, C. A. Biotechnological production of hyaluronic acid: a mini review. *3 Biotech* **6**, 67 (2016).
5. Di Mola, A., Landi, M. R., Massa, A., D'Amora, U. & Guarino, V. Hyaluronic acid in biomedical fields: new trends from chemistry to biomaterial applications. *Int. J. Mol. Sci.* **23**, 14372 (2022).
6. Liu, L., Liu, Y., Li, J., Du, G. & Chen, J. Microbial production of hyaluronic acid: current state, challenges, and perspectives. *Microb. Cell Fact.* **10**, 99 (2011).
7. Yu, H. & Stephanopoulos, G. Metabolic engineering of *Escherichia coli* for biosynthesis of hyaluronic acid. *Metab. Eng.* **10**, 24–32 (2008).
8. Jin, P., Kang, Z., Yuan, P., Du, G. & Chen, J. Production of specific-molecular-weight hyaluronan by metabolically engineered *Bacillus subtilis* 168. *Metab. Eng.* **35**, 21–30 (2016).
9. Puvendran, K. & Jayaraman, G. Enhancement of acetyl-CoA by acetate co-utilization in recombinant *Lactococcus lactis* cultures enables the production of high molecular weight hyaluronic acid. *Appl. Microbiol. Biotechnol.* **103**, 6989–7001 (2019).
10. Jeong, E., Shim, W. Y. & Kim, J. H. Metabolic engineering of *Pichia pastoris* for production of hyaluronic acid with high molecular weight. *J. Biotechnol.* **185**, 28–36 (2014).
11. Cai, N. et al. Engineering of the DNA replication and repair machinery to develop binary mutators for rapid genome evolution of *Corynebacterium glutamicum*. *Nucleic Acids Res.* **51**, 8623–8642 (2023).
12. Zha, J. et al. Biosystem design of *Corynebacterium glutamicum* for bioproduction. *Curr. Opin. Biotechnol.* **79**, 102870 (2023).
13. Becker, J., Rohles, C. M. & Wittmann, C. Metabolically engineered *Corynebacterium glutamicum* for bio-based production of chemicals, fuels, materials, and healthcare products. *Metab. Eng.* **50**, 122–141 (2018).
14. Wang, Y. et al. Eliminating the capsule-like layer to promote glucose uptake for hyaluronan production by engineered *Corynebacterium glutamicum*. *Nat. Commun.* **11**, 3120 (2020).
15. Cheng, F., Yu, H. & Stephanopoulos, G. Engineering *Corynebacterium glutamicum* for high-titer biosynthesis of hyaluronic acid. *Metab. Eng.* **55**, 276–289 (2019).
16. Hoffmann, J. & Altenbuchner, J. Hyaluronic acid production with *Corynebacterium glutamicum*: effect of media composition on yield and molecular weight. *J. Appl. Microbiol.* **117**, 663–678 (2014).
17. Du, Y., Cheng, F., Wang, M., Xu, C. & Yu, H. Indirect pathway metabolic engineering strategies for enhanced biosynthesis of hyaluronic acid in engineered *Corynebacterium glutamicum*. *Front. Bioeng. Biotechnol.* **9**, 768490 (2021).
18. Agarwal, G., K V, K., Prasad, S. B., Bhaduri, A. & Jayaraman, G. Biosynthesis of hyaluronic acid polymer: dissecting the role of sub structural elements of hyaluronan synthase. *Sci. Rep.* **9**, 12510 (2019).
19. DeAngelis, P. L. Molecular directionality of polysaccharide polymerization by the *Pasteurella multocida* hyaluronan synthase. *J. Biol. Chem.* **274**, 26557–26562 (1999).
20. DeAngelis, P. L., Jing, W., Drake, R. R. & Achyuthan, A. M. Identification and molecular cloning of a unique hyaluronan synthase from *Pasteurella multocida*. *J. Biol. Chem.* **273**, 8454–8458 (1998).
21. DeAngelis, P. L. & Zimmer, J. Hyaluronan synthases; mechanisms, myths, & mysteries of three types of unique bifunctional glycosyltransferases. *Glycobiology* **33**, 1117–1127 (2023).
22. Heldermon, C., DeAngelis, P. L. & Weigel, P. H. Topological organization of the hyaluronan synthase from *Streptococcus pyogenes*. *J. Biol. Chem.* **276**, 2037–2046 (2001).
23. Tlapak-Simmons, V. L., Baron, C. A. & Weigel, P. H. Characterization of the purified hyaluronan synthase from *Streptococcus equisimilis*. *Biochemistry* **43**, 9234–9242 (2004).
24. Weigel, P. H. Hyaluronan synthase: the mechanism of initiation at the reducing end and a pendulum model for polysaccharide translocation to the cell exterior. *Int. J. Cell Biol.* **2015**, 367579 (2015).
25. Kumari, K., Baggenstoss, B. A., Parker, A. L. & Weigel, P. H. Mutation of two intramembrane polar residues conserved within the hyaluronan synthase family alters hyaluronan product size. *J. Biol. Chem.* **281**, 11755–11760 (2006).
26. Weigel, P. H. & Baggenstoss, B. A. Hyaluronan synthase polymerizing activity and control of product size are discrete enzyme functions that can be uncoupled by mutagenesis of conserved cysteines. *Glycobiology* **22**, 1302–1310 (2012).
27. Yang, J. et al. Key role of the carboxyl terminus of hyaluronan synthase in processive synthesis and size control of hyaluronic acid polymers. *Biomacromolecules* **18**, 1064–1073 (2017).
28. Hu, L. et al. Biosynthesis of non-sulfated high-molecular-weight glycosaminoglycans and specific-sized oligosaccharides. *Carbohydr. Polym.* **295**, 119829 (2022).
29. DeAngelis, P. L., Papaconstantinou, J. & Weigel, P. H. Molecular cloning, identification, and sequence of the hyaluronan synthase gene from group A *Streptococcus pyogenes*. *J. Biol. Chem.* **268**, 19181–19184 (1993).
30. Heldermon, C. D., Tlapak-Simmons, V. L., Baggenstoss, B. A. & Weigel, P. H. Site-directed mutation of conserved cysteine residues does not inactivate the *Streptococcus pyogenes* hyaluronan synthase. *Glycobiology* **11**, 1017–1024 (2001).
31. Tlapak-Simmons, V. L., Baggenstoss, B. A., Kumari, K., Heldermon, C. & Weigel, P. H. Kinetic characterization of the recombinant hyaluronan synthases from *Streptococcus pyogenes* and *Streptococcus equisimilis*. *J. Biol. Chem.* **274**, 4246–4253 (1999).
32. Westbrook, A. W., Ren, X., Moo-Young, M. & Chou, C. P. Engineering of cell membrane to enhance heterologous production of hyaluronic acid in *Bacillus subtilis*. *Biotechnol. Bioeng.* **115**, 216–231 (2018).
33. Westbrook, A. W., Ren, X., Oh, J., Moo-Young, M. & Chou, C. P. Metabolic engineering to enhance heterologous production of hyaluronic acid in *Bacillus subtilis*. *Metab. Eng.* **47**, 401–413 (2018).
34. Maloney, F. P. et al. Structure, substrate recognition and initiation of hyaluronan synthase. *Nature* **604**, 195–201 (2022).
35. Harayama, T. & Riezman, H. Understanding the diversity of membrane lipid composition. *Nat. Rev. Mol. Cell Biol.* **19**, 281–296 (2018).
36. Martens, C., Shekhar, M., Lau, A. M., Tajkhorshid, E. & Politis, A. Integrating hydrogen-deuterium exchange mass spectrometry with molecular dynamics simulations to probe lipid-modulated conformational changes in membrane proteins. *Nat. Protoc.* **14**, 3183–3204 (2019).
37. Phillips, R., Ursell, T., Wiggins, P. & Sens, P. Emerging roles for lipids in shaping membrane-protein function. *Nature* **459**, 379–385 (2009).
38. Jumper, J. et al. Highly accurate protein structure prediction with AlphaFold. *Nature* **596**, 583–589 (2021).
39. Mandawe J. Engineering of hyaluronic acid synthases from *Streptococcus equi* subsp. *zooepidemicus* and *Pasteurella multocida* towards improved HA chain length and titer. <https://doi.org/10.18154/RWTH-2018-230230> (2022).
40. Navarro, P. P. et al. Cell wall synthesis and remodelling dynamics determine division site architecture and cell shape in *Escherichia coli*. *Nature. Microbiol.* **7**, 1621–1634 (2022).
41. Zhou, X. et al. Sequential assembly of the septal cell envelope prior to V snapping in *Corynebacterium glutamicum*. *Nat. Chem. Biol.* **15**, 221–231 (2019).

42. Kim, M. J., Yim, S. S., Choi, J. W. & Jeong, K. J. Development of a potential stationary-phase specific gene expression system by engineering of SigB-dependent cg3141 promoter in *Corynebacterium glutamicum*. *Appl. Microbiol. Biotechnol.* **100**, 4473–4483 (2016).
43. Baggenstoss, B. A. et al. Hyaluronan synthase control of synthesis rate and hyaluronan product size are independent functions differentially affected by mutations in a conserved tandem B-X7-B motif. *Glycobiology* **27**, 154–164 (2017).
44. Levental, I. & Lyman, E. Regulation of membrane protein structure and function by their lipid nano-environment. *Nat. Rev. Mol. Cell Biol.* **24**, 107–122 (2023).
45. Weigel, P. H. & DeAngelis, P. L. Hyaluronan synthases: a decade-plus of novel glycosyltransferases. *J. Biol. Chem.* **282**, 36777–36781 (2007).
46. Jiang, T., Li, C., Teng, Y., Zhang, R. & Yan, Y. Recent advances in improving metabolic robustness of microbial cell factories. *Curr. Opin. Biotechnol.* **66**, 69–77 (2020).
47. Ko, Y. S. et al. Tools and strategies of systems metabolic engineering for the development of microbial cell factories for chemical production. *Chem. Soc. Rev.* **49**, 4615–4636 (2020).
48. Lee, J. W. et al. Systems metabolic engineering of microorganisms for natural and non-natural chemicals. *Nat. Chem. Biol.* **8**, 536–546 (2012).
49. Chen, R. et al. Engineering cofactor supply and recycling to drive phenolic acid biosynthesis in yeast. *Nat. Chem. Biol.* **18**, 520–529 (2022).
50. Britton, B. M. et al. Conformational changes in the essential *E. coli* septal cell wall synthesis complex suggest an activation mechanism. *Nat. Commun.* **14**, 4585 (2023).
51. Zhou, H. et al. A citric acid cycle-deficient *Escherichia coli* as an efficient chassis for aerobic fermentations. *Nat. Commun.* **15**, 2372 (2024).
52. Eggeling, L., Bott, M. *Handbook of Corynebacterium Glutamicum*. (2005).
53. Bitter, T. & Muir, H. M. A modified uronic acid carbazole reaction. *Anal. Biochem.* **4**, 330–334 (1962).
54. Baek, M. et al. Accurate prediction of protein structures and interactions using a three-track neural network. *Science* **373**, 871–876 (2021).
55. Schindelin, J. et al. Fiji: an open-source platform for biological-image analysis. *Nat. Methods* **9**, 676–682 (2012).

## Acknowledgements

This work was financially supported by the National Key Research and Development Program of China (Grant No. 2024YFF1106300 to Z.K.), the National Natural Science Foundation of China (Grant No. U24A20368 to Z.K.), the Jiangsu Basic Research Center for Synthetic Biology (Grant No. BK20233003 to Z.K.), the Pilot Research Program of WIIRI (Grant No.

XD24006 to Z.K.) and the Research Program of State Key Laboratory of Food Science and Resources, Jiangnan University (Grant No. SKLF-ZZB-202418 to Z.K.).

## Author contributions

L.H. performed the experiments. Z.K. and L.H. designed the experiments. J.S. and W.X. contributed to the micrographs. S.X., F.W., and G.Y. contributed to the shake flask cultivation. Z.K. and L.H. analyzed data and drafted the manuscript. J., G.D., and J.H.C. modified the manuscript.

## Competing interests

The authors declare no competing interests.

## Additional information

**Supplementary information** The online version contains supplementary material available at <https://doi.org/10.1038/s41467-025-56950-3>.

**Correspondence** and requests for materials should be addressed to Zhen Kang.

**Peer review information** *Nature Communications* thanks Hyun Uk Kim, and the other anonymous reviewer(s) for their contribution to the peer review of this work. A peer review file is available.

**Reprints and permissions information** is available at <http://www.nature.com/reprints>

**Publisher's note** Springer Nature remains neutral with regard to jurisdictional claims in published maps and institutional affiliations.

**Open Access** This article is licensed under a Creative Commons Attribution-NonCommercial-NoDerivatives 4.0 International License, which permits any non-commercial use, sharing, distribution and reproduction in any medium or format, as long as you give appropriate credit to the original author(s) and the source, provide a link to the Creative Commons licence, and indicate if you modified the licensed material. You do not have permission under this licence to share adapted material derived from this article or parts of it. The images or other third party material in this article are included in the article's Creative Commons licence, unless indicated otherwise in a credit line to the material. If material is not included in the article's Creative Commons licence and your intended use is not permitted by statutory regulation or exceeds the permitted use, you will need to obtain permission directly from the copyright holder. To view a copy of this licence, visit <http://creativecommons.org/licenses/by-nc-nd/4.0/>.

© The Author(s) 2025